Simulation of the Kitagawa-Takahashi diagram using a probabilistic approach for cast Al-Si alloys under different multiaxial loads

Viet-Duc Le [a,b,c,*], Franck Morel [a], Daniel Bellett [a], Nicolas Saintier [b], Pierre Osmond [c]

[a] *Arts et Métiers ParisTech, CER Angers, Laboratoire LAMPA, 2 Bd du Ronceray, 49035 Angers Cedex 1, France*
[b] *Arts et Métiers ParisTech, CER Bordeaux, Laboratoire I2M, Esplanade des Arts et Mtiers, 33405 TALENCE Cedex, France*
[c] *PSA Peugeot Citroën, 18 rue des fauvelles, 92256 La Garenne-Colombes cedex, France*

ABSTRACT

This article describes a microstructural-based high cycle fatigue strength modelling approach applied to different cast Al-Si alloys used in an automotive context. Thank to different casting processes (gravity die casting and lost foam casting), associated with several heat treatment (T7 and Hot Isostatic Pressing-HIP), three alloys with very different microstructures have been obtained. In a vast experimental campaign undertaken to investigate the fatigue damage mechanisms governing these alloys under different multi-axial loading conditions, it was shown that the principal crack initiation mechanisms for the porosity-free alloy are either the formation of persistent slip bands (PSB) or the rupture and/or debonding of eutectic particles. For the porosity-containing alloys, the fatigue damage is always controlled by crack growth from pores. In order to take into account these fatigue damage mechanisms, a probabilistic model using a combination of the Dang Van and a modified LEFM criteria is proposed. The modified LEFM criterion is able to take into account the influence of the grain size on the threshold of the stress intensity factor.

It is shown that for the porosity-free alloy, the predictions are good for combined tension-torsion loads with $R = -1$. However, because the crack initiation mechanisms are not the same depending on the hydrostatic stress, the predictions are non-conservative for the uniaxial and equibiaxial tension loads with $R = 0.1$. For the porosity-containing alloys, the predictions are very good for the uniaxial, combined tension-torsion and equibiaxial tension loads with both $R = -1$ and $R = 0.1$. As observed experimentally, the proposed model can also predict a more pronounced effect of casting porosity for the uniaxial and combined tension-torsion loads, when compared to pure torsion loads.

1. Introduction

Cast aluminium alloys have been used to manufacture automotive components for many years due to their low density and excellent thermal conductivity. These components are subjected to cyclic mechanical loads which can cause fatigue damage and the functional failure of the structure. It has been demonstrated [1–6] that in high cycle fatigue (HCF), one of the principal parameters controlling the fatigue strength of cast Al-Si alloys is the presence of different microstructural heterogeneities which occur in the form of inclusions (Si particles and inter-metallics), casting defects (micro-shrinkage or degassing pores) and at the level of the aluminium matrix (often characterised by the DAS (Dendrite Arms Spacing) and/or SDAS (Secondary Dendrite Arms Spacing)

and the precipitation hardening level). These characteristics depend principally on the casting process (gravity die cast, lost foam cast, sand cast, etc.) as well as the post-heat treatment (T6/T7, hot isostatic pressing (HIP)). The object of this work is to develop a modelling approach which can take into account the effect of the casting processes and the associated heat treatments for different multiaxial loading conditions.

In the work of Koutiri et al. [7,8], the authors observed that the influence of casting porosity on the HCF strength of cast the AlSi7Mg03Cu05 alloy depends on the loading condition. It was shown that casting pores have a greater detrimental effect for uni-axial loads when compared to pure torsion loads, while the effect of biaxial tension is not detrimental for this porosity-containing alloy. A probabilistic model using the combination of the Huyen et al. [9] and the classical LEFM criteria was proposed to take into account these effects.

Based on this work, the principal aim of the present research is to decouple the roles of the different microstructural hetero-

geneities on the fatigue damage mechanisms and the fatigue strength of cast aluminium alloys. In order to achieve, an extensive multiaxial HCF testing campaign was conducted, including tension-compression loads with $R = -1$, pure torsion with $R = -1$, combined tension-torsion with $R = -1$, and equibiaxial loads with $R = 0.1$. Three different Al-Si alloys were investigated: (a) a gravity die cast alloy with a T7 heat treatment, designated **Alloy A** (this is the same alloy as the material investigated by Koutiri et al.) (b) a lost foam cast alloy with a T7 heat treatment, designated **Alloy B** and (c) a lost foam cast alloy with a HIP-T7 heat treatment, designated **Alloy C**. Thanks to these different processes, three very different micro-structures and casting defect populations have been obtained in order to highlight the roles of the different microstructural heterogeneities.

The experimental part of this work has been published in much greater detail elsewhere [10]. In particular, numerous fatigue damage observations have been presented for the three alloys. These observations revalidate the results obtained by Koutiri et al. [8,7], and link the fatigue behaviour to the fatigue damage mechanisms for the different multiaxial loading conditions, hence clarifying and decoupling the role of the different microstructural heterogeneities on the HCF behaviour.

In order to propose a criterion which can take into account the different casting processes and post-casting treatments, the modelling framework introduced by Pessard, Morel and co-workers will be used [11–15,5,8]. This approach leads naturally to a multiaxial, probabilistic Kitagawa-Takahashi type diagram. The model will be developed using a combination of the Dang Van criterion and a modified LEFM criterion to predict the influence of the couple (SDAS, grain size) on the fatigue strength.

2. Materials and experimental conditions

2.1. Casting processes and microstructural properties

The three hypo-eutectic Al-Si cast alloys under investigation are referred to as alloy A, B and C. These materials are also presented in a previous publication titled "*Multiaxial high cycle fatigue damage mechanisms associated with the different microstructural*

heterogeneities of cast aluminium alloys" [10]. The microstructures of these three materials are shown in Fig. 1.

Tables 1 and 2 summarise the chemical composition, the casting process and the post-cast treatment as well as the microstructural and mechanical properties of these alloys. The details relating to the casting processes, the preparation of the fatigue specimens as well as the methodologies used for the microstructural characterisation are discussed in reference [10].

It must be kept in mind that alloy A contains an additional 0.5 wt% copper, compared to alloys B and C. The presence of cooper results in a higher micro-hardness of the alpha phase (see Table 2).

2.2. Pore size distribution characterisation

2.2.1. Surface characterisation of pore size distribution

In order to characterise the size distribution of the casting defect, the extreme value inclusion rating methodology, proposed by Murakami [16], has been used. The defect size distribution is determined from optical microscopic observations of polished samples. In particular, the maximum defect size $\sqrt{area_{max,j}}$ in each standard inspection $area_j$ of size $S_0 = 2.5 \text{ mm}^2$, is measured (see Fig. 2(a)). The cumulative probability function F_j is calculated by:

$$F(\sqrt{area_{max,j}}) = F_j = \frac{j}{n+1} \tag{1}$$

The defect size distributions of the three alloys are shown in Fig. 2(b). The Gumbel distribution is used to fit the experimental data. Greater detail concerning this methodology can be found in the published paper [10].

2.2.2. Possibility of prediction maximum pore size

One of the advantages of this methodology is the possibility of predicting the maximum defect size in a given volume. Firstly, the reduced variable y_j corresponding to each measured pore size $\sqrt{area_{max,j}}$ is calculated by Eq. (2). If the defect size distribution is a good fit with the Gumbel distribution, the relationship between the reduced variable y_j and the defect size $\sqrt{area_{max,j}}$ will be linear.
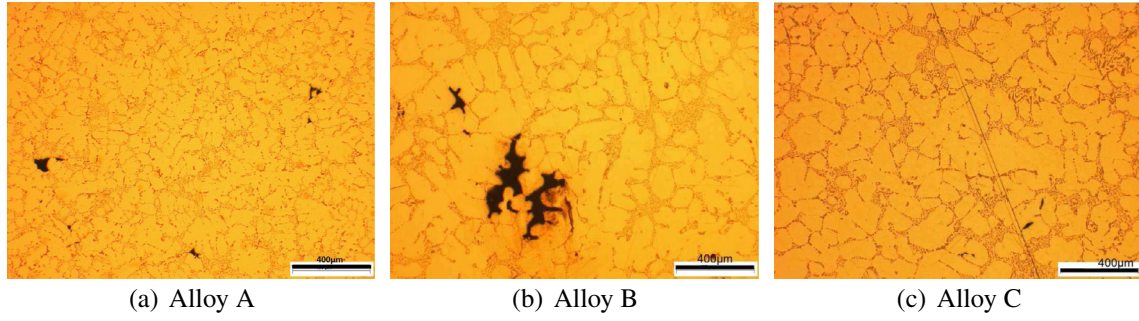
(a) Alloy A   (b) Alloy B   (c) Alloy C

Fig. 1. Microstructures of three alloys under investigation.

Table 1
Chemical composition, casting process and heat treatment of the three studied material (HIP = Hot Isostatic Pressing.

Alloy	Chemical composition (wt.)	Casting process	Heat treatment
A	7%Si, 0.3%Mg, 0.5%Cu, Remainder Al	Gravity Die Cast	T7
B	7%Si, 0.3%Mg, Remainder Al	Lost Foam Cast	T7
C	7%Si, 0.3%Mg, Remainder Al	Lost Foam Cast	HIP + T7

Table 2
Mean value and standard deviation of the SDAS, the grain size, the micro-hardness of the aluminium matrix and the yield strength of the three alloys being investigated.

Alloy	SDAS $[\mu \pm s]$ (μm)	Grain size $\sqrt{area_g}$ $[\mu \pm s]$ (μm)	Micro-hardness $[\mu \pm s]$ (Hv0.025)	Yield strength $R_{p0.2\%}$ $[\mu \pm s]$ (MPa)
A	42.3 ± 9.7	298 ± 126	113.8 ± 2.8	260.4 ± 1.6
B	77.3 ± 18.9	N/A	99 ± 9	240.1 ± 4.5
Heyder C	91.4 ± 32.8	411 ± 197	92 ± 13	250.2 ± 3.4

$$y_j = -\ln\left[-\ln\left(F_j\right)\right] = -\ln\left[-\ln\left(\frac{j}{n+1}\right)\right] \tag{2}$$

In order to predict the maximum defect size in a given volume V, the "return period" T defined by Eq. (3) is used.

$$T = \frac{V}{V_0} \tag{3}$$

where V_0 is the standard inspection volume, which can be estimated from the standard inspection area S_0 by assuming that the thickness, h, of the standard inspection volume is $h = \left(\sum_{n} \sqrt{area_{max,j}}\right)/n$ where n is the total number of standard inspection areas. The reduced variable related to the volume V is then calculated by following equation:

$$y_T = -\ln\left[-\ln\left(\frac{T-1}{T}\right)\right] \tag{4}$$

The application of this methodology is shown in Fig. 3. Note that two volumes V are considered: the first is the total loaded volume in the fatigue specimens (i.e. a cylinder of diameter 7 mm with a height of 10 mm). The second volume considered corresponds to the sub-surface volume. The reason for considering this volume is that experimentally it is observed that all principal fatigue cracks initiate from the surface or sub-surface pores. The thickness of the sub-surface volume is assumed to be the maximum defect size observed on the fatigue failure surfaces or 500 μm approximately.

It can be observed that the difference between the predictions related to the total loaded volume and the ones related to the sub-surface volume is not significant. The predicted maximum pore size in loaded volume is between 202 μm and 255 μm for alloy A; between 635 μm and 700 μm for alloy B. Regarding alloy C, the maximum pore size is around 50 μm. These predictions for alloys A and B are in a good agreement with the average size of pores observed on the failure surfaces in the crack initiation zone (of fatigue specimens tested under uniaxial and combined tension-torsion loads), presented later in Table 4.
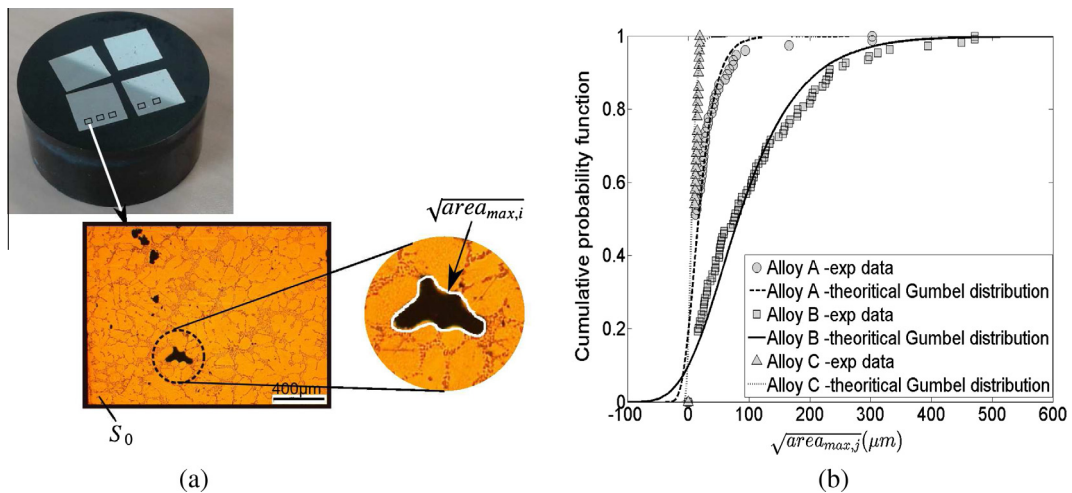

(a)   (b)

Fig. 2. (a) Extreme value inclusion rating methodology for the characterisation of the defect size distribution and (b) Defect size distributions for the three alloys under investigation.
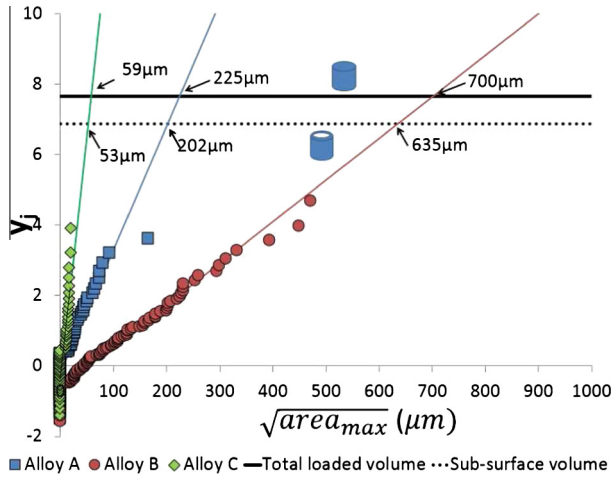
Fig. 3. Prediction of the maximum defect size in a given volume. Two volumes are concerned in the prediction: the total loaded volume (continuous line) and the sub-surface volume (dashed line) in the fatigue specimen.

This result is very encouraging and leads to the possibility of developing a methodology to predict the fatigue strength which could take into account the volume effect using an extreme value defect rating methodology. This will be investigated in future work, however the strategy here is to avoid volume effects by using the same or similar specimen geometries in the experimental work.

2.3. Fatigue test conditions

All of the fatigue tests presented below were carried out at ambient temperature and pressure in laboratory air. The fatigue tests under uniaxial loads, torsion loads and combined tension-torsion loads ($k = \tau_{xy,a}/\sigma_{xx,a} = 0.5$) with a load ratio of $R = -1$ were conducted with the specimen geometry shown in Fig. 4(a) (except for the fatigue tests conducted by Koutiri et al. [7] in plane bending with alloy A). The fatigue tests for equibiaxial tension loads with $R = 0.1$ were carried out with the disk shaped specimens introduced by Koutiri et al. [7] (see Fig. 4(b)). All of the fatigue specimens were mechanically mirror polished. The fatigue tests were conducted using the staircase technique with 20 specimens. A maximum fatigue life of 2×10^6 cycles was used. The stopping

criteria were chosen to ensure the presence of a fatigue crack of approximately 3 mm in length. Greater detail concerning these tests can be found in Refs. [10,7].

3. High cycle fatigue behaviour and the associated damage mechanisms

The fatigue strength at 2×10^6 cycles of the three alloys is presented in Table 3.

Fig. 5 summarises the fatigue damage mechanisms observed in the three studied alloys for uniaxial loads with $R = -1$, torsion loads with $R = -1$ and combined tension-torsion ($k = \tau/\sigma = 0.5$) with $R = -1$. Greater details concerning the fatigue strength analysis as well as the observations of the fatigue damage mechanisms can be found in [10].

This figure highlights that:

- For uniaxial tensile loads and combined tension-torsion loads with $R = -1$: fatigue cracks always initiate and propagate from pores for the porosity-containing materials (alloys A and B). However, for the porosity-free alloy (alloy C), fatigue cracks initiate from persistent slip bands (PSBs).
- For torsion loads with $R = -1$: two crack initiation mechanisms have been observed: the first mechanism is related to crack propagation from pores located on the specimen surface and the second is controlled by PSB formation. These two mechanisms coexist and have been observed on the same specimen. For the porosity-free alloy (alloy C), only crack initiation via PSB formation was observed.

Concerning the equibiaxial tension loads with $R = 0.1$, it was seen that the principal fatigue damage mechanism for the porosity-containing alloys (alloys A and B) is crack growth from pores [7]. For the porosity-free alloy (alloy C) fatigue crack initiation for equibiaxial tension loads with $R = 0.1$ is controlled by the rupture and/or debonding of the eutectic particles (i.e. Si particles, intermetallic inclusions) (see Fig. 6). This is contrary to the uniaxial case with $R = -1$ in which the formation of PSB was observed.

In order to decouple the effect of the stress biaxiality and the mean stress effect on the crack initiation mechanism for alloy C, four uniaxial fatigue tests at $R = 0.1$ were carried out. A competition between the two aforementioned initiation mechanisms was observed. The first mechanism being PSB formation and the second

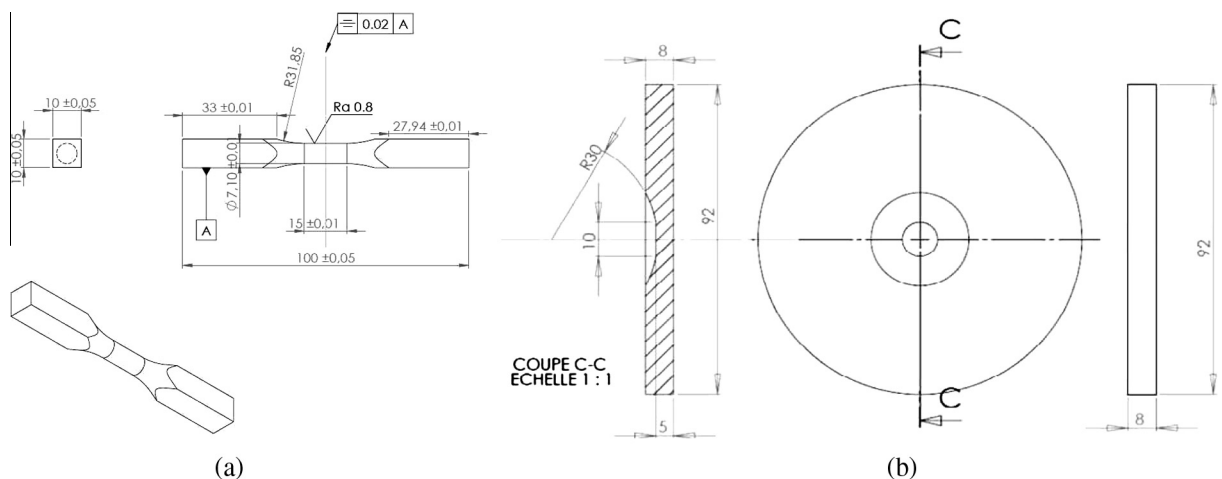(a)   (b)

Fig. 4. (a) The fatigue specimen geometry for the uniaxial tests ($R = -1$), the torsion ($R = -1$) and the combined tension-torsion tests ($R = -1$) and (b) the specimen geometry for the equib-iaxial tests ($R = 0.1$) [7].

Loading condition	Fatigue strength amplitude σ_a [$\mu \pm s$] (MPa)		
	Alloy A	Alloy B	Alloy C
Uniaxial $R = -1$	83 ± 18 [7]	65 ± 13	126 ± 13
Torsion $R = -1$	93 ± 14 [7]	69 ± 5	72 ± 8
Combined tension-torsion $R = -1$	66 ± 13	49 ± 10	80 ± 5
Uniaxial $R = 0.1$	63 ± 15 [7]	N/A	N/A
Equibiaxial tension $R = 0.1$	63 ± 5 [7]	46 ± 5	68 ± 5

concerning the rupture/debonding of eutectic particles. This competition was also observed in the work of Dezecot and Brochu [17]. By considering the maximum hydrostatic stress for each loading condition, **it can be seen that an increase of the maximum hydrostatic stress can lead to a change of damage mechanism, from the crack initiation by the PSB formation to the crack initiation by the rupture and/or debonding of the eutectic particles**.

4. Modelling framework and application to the cast alloys being investigated

4.1. The probabilistic concept for fatigue strength modelling

Initiated by Pessard and Morel [11–15,5,8], the probabilistic modelling framework used below was initially proposed to describe the competition between two different fatigue crack damage mechanisms in a bainitic steel: one related to local plasticity at the mesoscopic scale and the other controlled by crack growth from clusters of MnS inclusions. In order to describe these mechanisms in a high cycle fatigue strength model, the authors determine the probability of failure in the material matrix Pf_1 and the probability of a crack propagating from MnS inclusion clusters Pf_2. The weakest link concept [18,19] can then be used to

determine the overall probability of survival of the specimen, referred to as Pf:

$$1 - Pf = (1 - Pf_1)(1 - Pf_2) \tag{5}$$

The expressions for Pf_1 and Pf_2 can be obtained using any two appropriate fatigue criteria such as the Crossland and Murakami criteria in the work of Pessard et al. [13] or the Nguyen [20] and an LEFM-based criteria in the work of Koutiri et al. [8].

4.2. Application to the cast aluminium alloys being investigated

In Section 3, it was shown that for the porosity-free alloy (alloy C), fatigue crack initiation is principally controlled by the formation of persistent slip bands in the aluminium matrix for the loading conditions with $R = -1$ (i.e. for low hydrostatic stress conditions) while for the equibiaxial tension loads with $R = 0.1$, the crack initiation is controlled by the rupture/debonding of the silicon particles and/or the intermetallic inclusions. However, for the porosity-containing alloys (alloys A and B), fatigue cracks initiate principally from casting pores. These observations suggest that the probabilistic concept presented in the previous section would be a reasonable choice to model the fatigue behaviour of the cast aluminium alloys under investigation.

4.2.1. Modelling of mechanism 1: crack initiation related to the formation of PSB
4.2.1.1. Modelling framework. As a first step, the Dang Van [21] criterion is chosen to describe the mechanism 1 related to the crack initiation in the aluminium matrix. As per the Dang Van criterion, it is assumed that the crack initiation can be modelled as the localisation of plasticity at the mesoscopic scale (i.e. the scale of individual grains). Hence, the crack initiation condition can be defined by Eq. (6):

$$\sigma_{DV} \geqslant \sigma_{th} \tag{6}$$

where σ_{DV} is the Dang Van equivalent stress and σ_{th} is the threshold stress. The Dang Van equivalent stress is computed by Eq. (7).
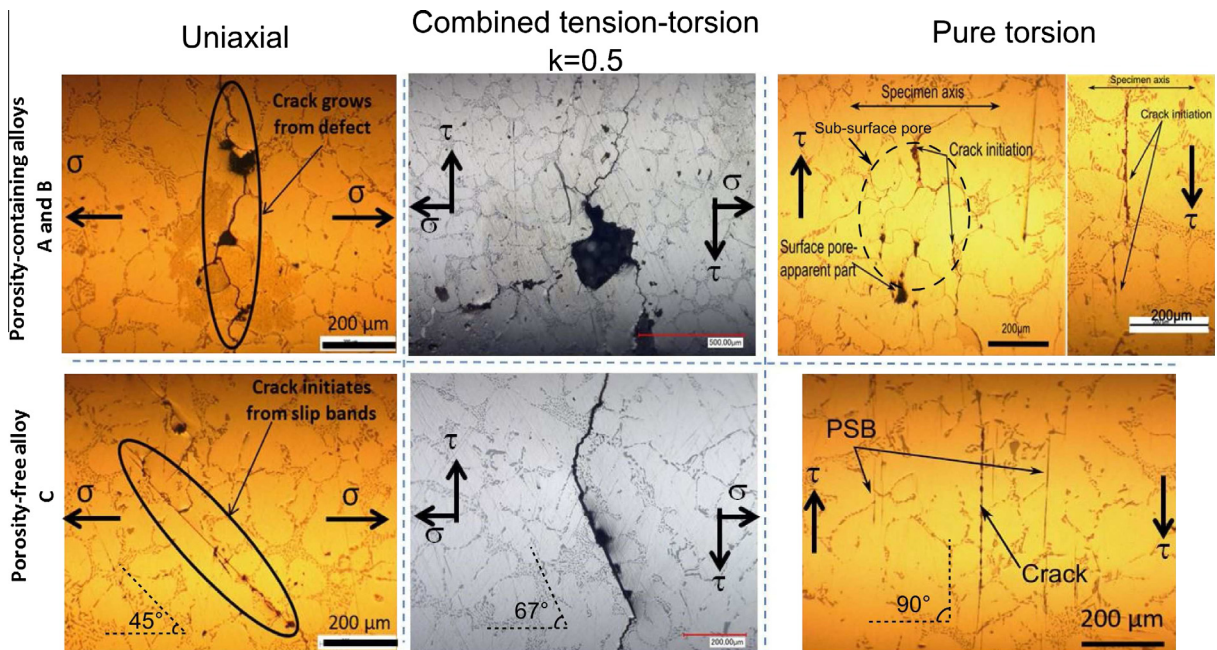

Fig. 5. Fatigue damage mechanisms of alloys A, B and C for three loading modes (pure tension with $R = -1$, combined tension-torsion with $R = -1$ and pure torsion with $R = -1$), observed on specimen surfaces.
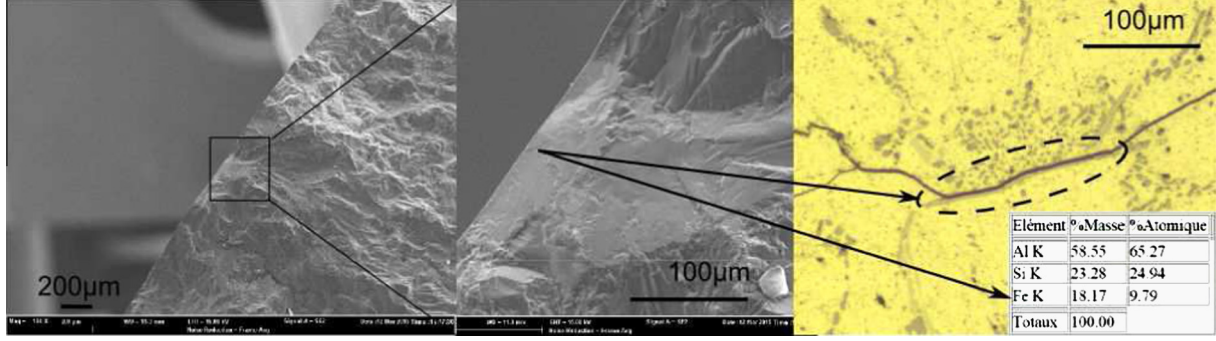
Fig. 6. Crack initiation caused by the rupture and/or debonding of the eutectic particles for the porosity-free alloy (alloy C) for equibiaxial tension loads with $R = 0.1$.

$$\sigma_{DV} = \max_{n\to}(\max_t(\tau + \alpha_{DV}\sigma_H)) \tag{7}$$

In order to take into account the fatigue strength scatter, a two-parameter Weibull distribution [19,18] is used to describe the dispersion associated with the stress threshold σ_{th}:

$$f_{01}(\sigma_{th}) = \frac{m_1}{\sigma_{th0}}\left(\frac{\sigma_{th}}{\sigma_{th0}}\right)^{m_1-1}\exp\left(-\left(\frac{\sigma_{th}}{\sigma_{th0}}\right)^{m_1}\right) \tag{8}$$

where σ_{th0} is the scale parameter and m_1 is the shape parameter of the distribution. The probability of finding a grain in which a fatigue crack is initiated can be expressed as:

$$Pf_{01}(\sigma_{th} < \sigma_{DV}) = \int_0^{\sigma_{DV}} f_{01}(\sigma_{th})d\sigma_{th} \tag{9}$$

Hence, the probability of crack initiation in an isolated grain is:

$$Pf_{01} = 1 - \exp\left(-\left(\frac{\sigma_{DV}}{\sigma_{th0}}\right)^{m_1}\right) \tag{10}$$

To calculate the global probability of failure of the structure for this fatigue damage mechanism, it is sufficient to sum the failure probabilities for each of the grains contained in the total loaded volume V (i.e. the weakest link theory [19]). This theory assumes that there is no interaction between crack initiation sites. Hence, the failure probability for damage mechanism 1 is described by:

$$Pf_1 = 1 - \prod_{M \in V}(1 - P_{F_{01}}) \tag{11}$$

$$\Rightarrow Pf_1 = 1 - \exp\left(-\frac{1}{V_{01}}\int_V\left(\frac{\sigma_{DV}}{\sigma_{th0}}\right)^{m_1}d_S\right) \tag{12}$$

where V_{01} is the volume of a grain (or the reference volume). When the stress field is uniform in the loaded volume, this expression can be simplified to:

$$Pf_1 = 1 - \exp\left(-\frac{V}{V_{01}}\left(\frac{\sigma_{DV}}{\sigma_{th0}}\right)^{m_1}\right) \tag{13}$$

By replacing $\sigma_{th0}\left(\frac{V_{01}}{V}\right)^{1/m_1}$ with σ_{th0}, the probability of failure associated with damage mechanism 1 is given by:

$$Pf_1 = 1 - \exp\left(-\left(\frac{\sigma_{DV}}{\sigma_{th0}}\right)^{m_1}\right) \tag{14}$$

4.2.2. Modelling of mechanism 2: fatigue damage associated with casting pores
4.2.2.1. Choice of fatigue strength criterion.
In order to choose an appropriated fatigue criterion to model the mechanism 2, it is analysed here the evolution of the uniaxial fatigue strength $\sigma_{xx,a}$ as a function of the experimentally determined pore size, in terms of the Murakami parameter $\sqrt{area}$, for three porosity containing alloys: alloys A, B and a third data set corresponding to fatigue tests conducted on specimens with the same chemical composition and heat treatment as Alloy A. This material was gravity-sand cast in the form of bars Bellett and Morel [22] and has approximately the same SDAS as alloy A and it is assumed that the grain size is also the similar.

Regarding the pore size, Table 4 resumes the mean pore size and the associated standard deviation of pores observed on the fatigue failure surfaces for different loading conditions. Fig. 7 shows an example of measuring a pore at the origin of the principal crack initiation observed on the failure surface. Note that for alloy B loaded in torsion, because crack initiation and propagation for some specimens is controlled by the same mechanism (i.e. controlled by the shear stress), the identification of the crack initiation site is very difficult. In this case the pore size corresponds to the largest pore observed on the failure surface.

Fig. 8 shows the relationship between the uniaxial fatigue strength and the pore size. Note that the vertical error bars correspond to a probability of failure of 10–90% and the horizon error bars indicate a probability of occurrence of 10–90% for the defect size. For the third data set Bellett and Morel [22], because the fatigue strength at 2×10^6 cycles was estimated from a Wöhler curve, the error bar for the fatigue strength has not been reported. The experimental data are compared to the fatigue strength predictions using the LEFM criterion in which the stress intensity threshold has been arbitrarily estimated to fit the experimental data. The LEFM criterion is described by Eq. (15).

$$\Delta K_{th} = 2\sigma_{xx,a}Y\sqrt{\pi\sqrt{area}} \tag{15}$$

Table 4
Mean defect size and associated standard deviation of pores at the origin of the principal fatigue cracks observed on the fatigue failure surfaces for different loading conditions. Note that for alloy C under the equibiaxial tension loads $R = 0.1$, the reported defect size correspond to the size of the eutectic inclusions at the crack initiation site.

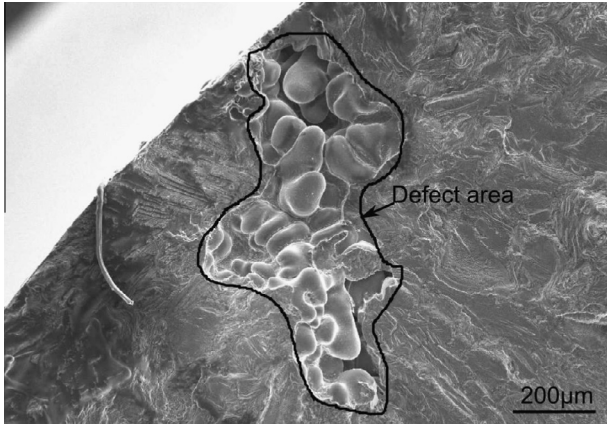| Loading condition	Mean value and standard deviation of defect size $\sqrt{area}$ (μm)			
	Alloy A	Alloy B	Alloy C	Alloy Bellett and Morel [22]
Uniaxial $R = -1$	235 ± 87	595 ± 260	No pore found	N/A
Torsion $R = -1$	N/A	690 ± 400	No pore found	N/A
Combined tension-torsion $R = -1$	209 ± 59	669 ± 457	No pore found	N/A
Uniaxial $R = 0.1$	N/A	N/A	N/A	709 ± 365
Equibiaxial tension $R = 0.1$	N/A	892 ± 407	76 ± 32	N/A

Fig. 7. Size measurement of a pore at the origin of the crack initiation.

where Y is the Murakami crack-shape factor and is equal to 0.65 for an arbitrary-shaped surface crack [16]. $\sigma_{I,a}$ is the uniaxial fatigue strength amplitude with $R = -1$ and $\sqrt{area}$ is the Murakami size parameter of the pores at the origin of the principal fatigue cracks. The values of ΔK_{th} are arbitrarily estimated to match the experimental data. As a comparison, the estimated $\Delta K_{th} \approx 2.2$ MPa$\sqrt{m}$ (for $R = 0.1$) is much lower than the growth threshold of **long cracks** reported in the literature [23–27] which is between 4 and 5.5 MPa$\sqrt{m}$ (obtained thank to long crack growth test under uniaxial loads at $R = 0.1$). This fact highlights the significant effect of small crack and/or crack closure of the fatigue natural cracks.

In Fig. 8, by comparing the experimental data for alloy A and the data obtained by Bellett et al., it can be seen that, for the alloys with the same microstructure (i.e. SDAS and/or grain size and chemical composition), the slope of the relationship "fatigue strength-pore size" in the log-log scale is approximately 1/2 for either $R = -1$ or $R = 0.1$. This trend suggests that the LEFM criterion could be appropriated to describe the evolution of the fatigue strength as a function of the pore size for alloys with the same microstructure. Furthermore, by comparing the fatigue strength of alloys A and Bellett et al. for two loading ratio $R = -1$ and $R = 0.1$, the effect of loading ratio R can be withdrawn.

The comparison between the three alloys for a load ratio of $R = -1$ shows that the stress intensity threshold for alloy B is slightly higher than the two other alloys. It is assumed that this difference is caused by the fact that alloy B has a larger SDAS and/or

grain size. In order to consolidate this assumption, crack growth data from the literature [23–27] is analysed in Fig. 9. This figure shows the evolution of the stress intensity threshold for long cracks as a function of different material properties such as the yield strength, the ultimate tensile strength, the percentage of copper and the SDAS. The data estimated from the fatigue strength and pore size issue from the present study (by Eq. (15)) are also presented. This figure indicates that there is a directly proportional relationship between the SDAS and ΔK_{th}. That is, an increase in the SDAS results in an higher stress intensity threshold. It can also be seen that this effect is the same for long cracks as well as for fatigue natural cracks growing from pores. It should be keep in mind that for the alloys under investigation, the SDAS and grain size are proportional and that this is also true for cast Al-Si alloys whose SDAS and grain size are controlled by a change of cooling rate [28]. Hence, from this data no distinction can be made between the SDAS and the grain size.

A possible explanation for the effect of the couple (SDAS, grain size) on ΔK_{th} of **the fatigue natural crack** is proposed below and is based on the experimental crack growth observations reported in the work of Munoz [29]. Fig. 10 shows the evolution of two natural fatigue cracks growing from pores in an A356-T6 alloy, loaded in uniaxial tension with $R = 0.1$ and $\sigma_{max} = 163$ MPa. Based on these observations, Serrano et al. state that the presence of grain boundaries decelerates the crack growth. However, it can also be seen that the early stage crack growth rate in the intergranular mode (Fig. 10-1 and 2) is much faster than in the intragranular mode (Fig. 10-3 and 4). From this point of view, it would not be unreasonable to assume that grain boundaries play multiple roles: the role of decelerating the crack growth when the crack become larger than the grain size and **the role of accelerating the early stage crack growth (i.e. when the crack length is less than the grain size)**. For the alloys investigated here, **because of relative large grain size compared to pore size, it can be assumed that the size of arrested cracks is smaller than the grain size**. Consequently, for non-propagating cracks, early stage crack growth is dominant and the principal role of the grain boundaries is to accelerate crack growth. Hence, it can be stated that an increase in the couple (SDAS, grain size), while conserving the defect size, leads to a decrease in the number of grain boundaries emanating from a pore which are favourable in terms of the loading direction. This diminution in turn forces the fatigue cracks to initiate and to micro-propagate in **intragranular** mode. Resulting from the relatively low crack growth rate of this mode (compared to the **intergranular** mode), the stress intensity threshold can increase. Fig. 11 illustrates graphically this explanation.
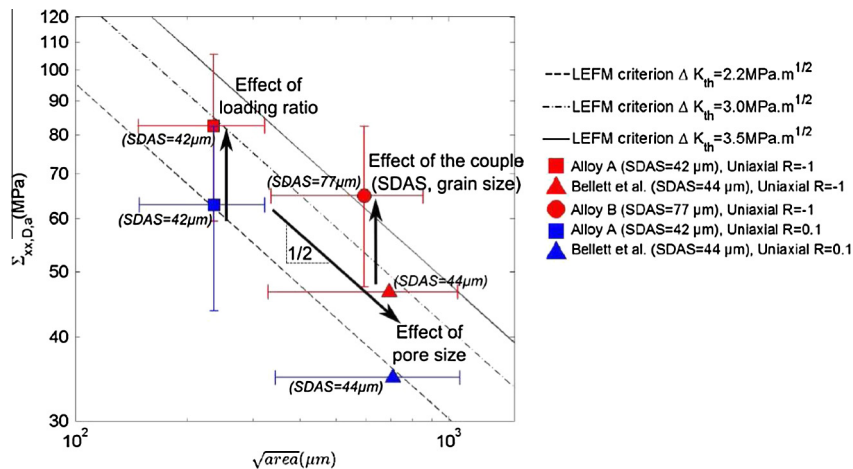

Fig. 8. Relationship between the uniaxial fatigue strength and the defect size at the origin of the principal fatigue cracks observed on the failure surfaces.
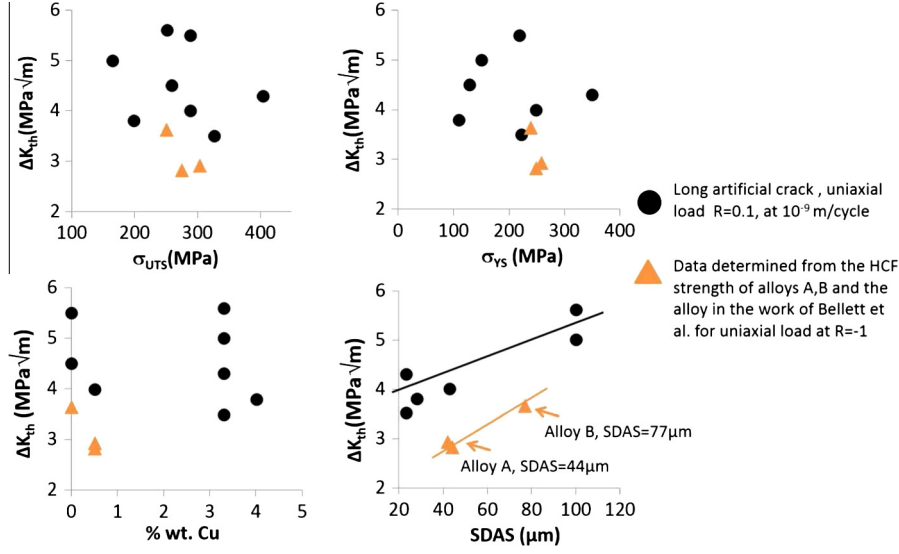
Fig. 9. The relationship between the stress intensity threshold and different material properties. The black points correspond to the literature data [23–27].

In conclusion, the LEFM criterion will be used to model the damage mechanism related to crack growth from pores. Because of the significant effect of small crack and/or crack closure related of the fatigue natural cracks growing from a pore, the value ΔK_{th} is determined from the pore size observed on failure surfaces and the related fatigue strength (by Eq. (15)). Furthermore, the influence of the grain size on the stress intensity threshold will be included in the proposed model.

4.2.2.2. Modelling framework. As per the LEFM approach, it is assumed that cracks will propagate if the following condition is satisfied:

$$\Delta K \geqslant \Delta K_{th} \tag{16}$$

By analogy with the first mechanism (see Eq. (8)), the Weibull distribution is used to describe the scatter associated with the threshold of the stress intensity factor:

$$f_{02}(\Delta K_{th}) = \frac{m_2}{\Delta K_{th0}} \left(\frac{\Delta K_{th}}{\Delta K_{th0}} \right)^{m_2-1} \exp\left[-\left(\frac{\Delta K_{th}}{\Delta K_{th0}} \right)^{m_2} \right] \tag{17}$$

where m_2 is the shape parameter and ΔK_{th0} is the scale factor.

Hence, the probability of crack growth from an individual pore can be expressed by:

$$Pf_{02} = 1 - \exp\left(-\left(\frac{\Delta K}{\Delta K_{th0}} \right)^{m_2} \right) \tag{18}$$

The probability of failure for the total volume can be expressed by following equation, given that the stress field is uniform in the loaded volume:

$$Pf_2 = 1 - \exp\left(-\left(\frac{\Delta K}{\Delta K'_{th0}} \right)^{m_2} \right) \tag{19}$$

where $\Delta K'_{th0} = \Delta K_{th0} \left(\frac{V_{02}}{V} \right)^{1/m_2}$ and V_{02} is the representative volume of a crack emanating from an individual pore.

4.2.3. Parameters identification
4.2.3.1. Material parameters related to the mechanism 1. The experimental fatigue data of alloy C is used to identify the material parameters related to the mechanism 1 because this alloy is porosity free and the mechanism 1 (i.e. the fatigue crack initiation in the aluminium matrix) is dominant (see Section 3).

- The shape factor m_1 is determined by the following equation where $\overline{\tau}_{-1,C}$ and $\overline{\overline{\tau}}_{-1,C}$ are respectively the mean value and the standard deviation of the experimentally determined pure torsion fatigue strength ($R = -1$) of alloy C (i.e. porosity-free alloy):

$$\frac{\overline{\overline{\tau}}_{-1,C}}{\overline{\tau}_{-1,C}} = \frac{\sqrt{\Gamma\left(1 + \frac{2}{m_1}\right) - \Gamma^2\left(1 + \frac{1}{m_1}\right)}}{\Gamma\left(1 + \frac{1}{m_1}\right)} \Rightarrow m_1 = 11.27 \tag{20}$$

- The Dang Van coefficient α_{DV} is determined using the following equation where $\overline{s}_{-1,C}$ is the mean value of the pure tension ($R = -1$) fatigue strength of alloy C:

$$\alpha_{DV} = \frac{\overline{\tau}_{-1,C} - \frac{\overline{s}_{-1,C}}{2}}{\frac{\overline{s}_{-1,C}}{3}} = 0.2049 \tag{21}$$

- The scale factor σ'_{th0} can be determined from the experimental data for the torsional fatigue strength of alloy C with $R = -1$ by the following equation:

$$\sigma'_{th0} = \frac{\overline{\tau}_{-1,C}}{\Gamma\left(1 + \frac{1}{m1}\right)} = 74 \text{ MPa} \tag{22}$$

4.2.3.2. Material parameters related to the mechanism 2. The experimental fatigue data of alloys A/B are used to identify the material parameters related to the mechanism 2 because these alloys are porosity containing and the mechanism 2 (i.e. the fatigue crack initiation induced by the porosity) is dominant (see Section 3).

- The shape factor m_2 is identified thank to the mean fatigue strength value, $\overline{s}_{-1,A/B}$, and the associated standard deviation, $\overline{\overline{s}}_{-1,A/B}$, for uniaxial loads with $R = -1$ of alloys A or B by the following equation:

$$\frac{\overline{\overline{s}}_{-1,A/B}}{\overline{s}_{-1,A/B}} = \frac{\sqrt{\Gamma\left(1 + \frac{2}{m_2}\right) - \Gamma^2\left(1 + \frac{1}{m_2}\right)}}{\Gamma\left(1 + \frac{1}{m_2}\right)} \tag{23}$$

A value of $m_2 = 5.37$ is obtained for alloy A and $m_2 = 5.59$ for alloy B.

- The scale factor $\Delta K'_{th0}$ can be determined by the following equation:
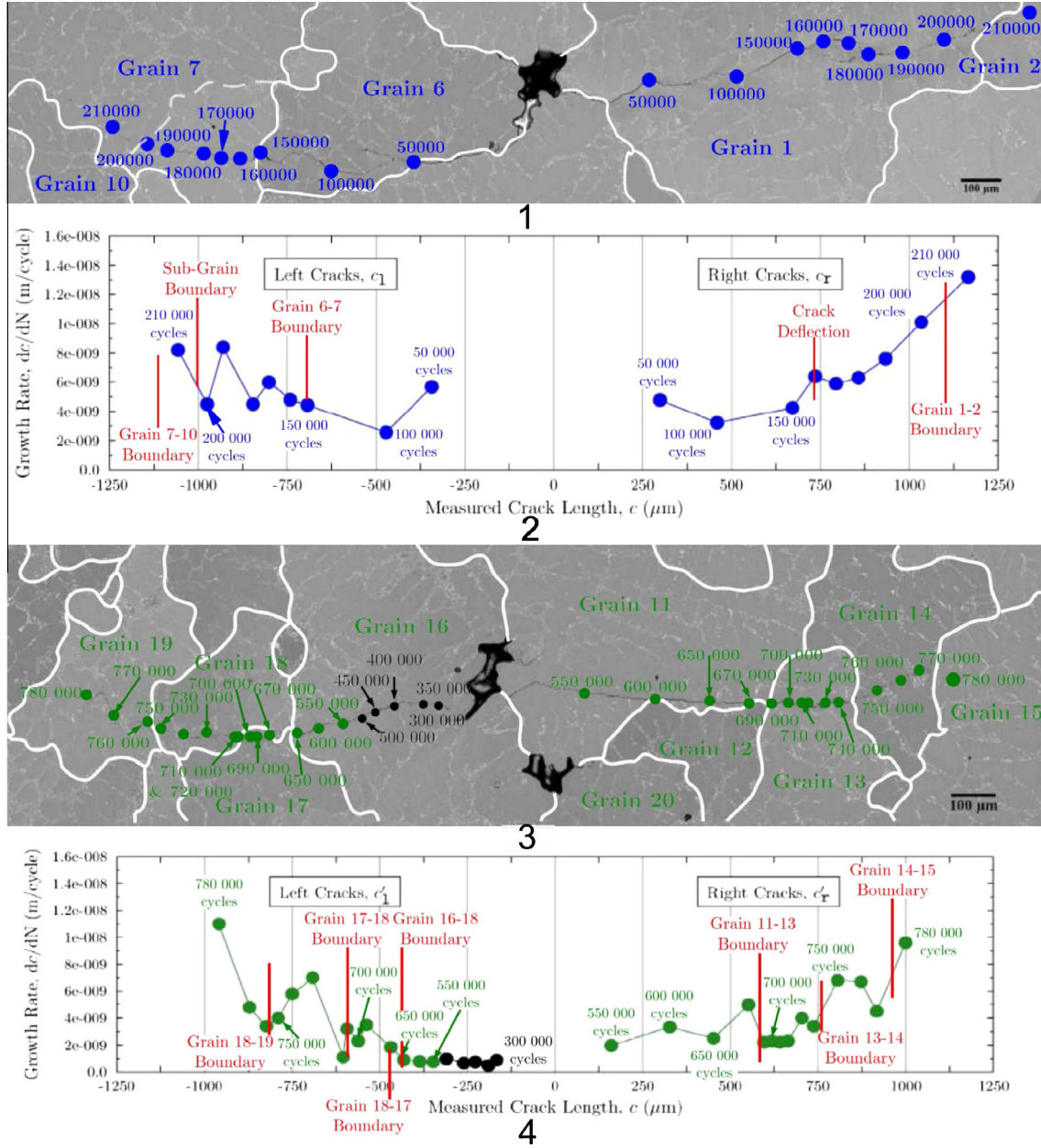
Fig. 10. Observations of two cracks growing from casting pores under the uniaxial loads with $R = 0.1$ and $\sigma_{max} = 163$ MPa, Munoz [29].

$$2\bar{s}_{-1,A/B} \times 0.65\sqrt{\pi\sqrt{area_{A/B}}} = \Delta K'_{th0}\Gamma\left(1 + \frac{1}{m_2}\right) \qquad (24)$$

where $\sqrt{area_{A/B}}$ corresponds to the mean value of the Murakami parameter determined for the pores in the crack initiation zones of alloy A or B (see Table 4). A value of $\Delta K'_{th0} = 3.1$ MPa $\sqrt{m}$ is obtained for alloy A and $\Delta K'_{th0} = 3.95$ MPa $\sqrt{m}$ for alloy B.

4.3. Results and discussions

4.3.1. The Dang Van and classical LEFM criteria combination

Firstly, the combination of the Dang Van and the classical LEFM criteria is presented. The correlation between the experimental fatigue strength and the model predictions for different loading conditions, presented in the form of Kitagawa-Takahashi diagrams, is shown in Fig. 12. In this diagram, the mechanism 1 is not influenced by the defect size area. Hence, a modelling approach, which only base on mechanism 1, would result in a horizontal line in

Fig. 12. Only the mechanism 2 depends on the defect size. The stress amplitude increases with decreasing defect size. The combination of both mechanisms (by Eq. (5)) leads to the predicted fatigue strength values displayed in Fig. 12. Note that for alloy C, because no pores were found on the fatigue failure surfaces, the defect size shown in the figure corresponds to the maximum defect size observed on polished samples using an optical microscope ($\sqrt{area} = 20$ μm). The vertical error bars correspond to a probability of failure of 10–90%. The horizontal bars correspond to the probability of occurrence of 10–90% for the defect size. The defect sizes measured in the crack initiation zones for the different loading conditions are resumed in Table 4. The data for alloy A loaded in torsion $R = -1$, uniaxial tension $R = 0.1$ and equibiaxial tension $R = 0.1$ loadings is from the work of Koutiri et al. [8] and the defect sizes were not reported. Hence, in Fig. 12 the defect size for these data points is assumed to be the same as the uniaxial case with $R = -1$.

Regarding the model predictions including a mean stress (i.e. with $R = 0.1$), the influence of the load ratio, R, on the stress
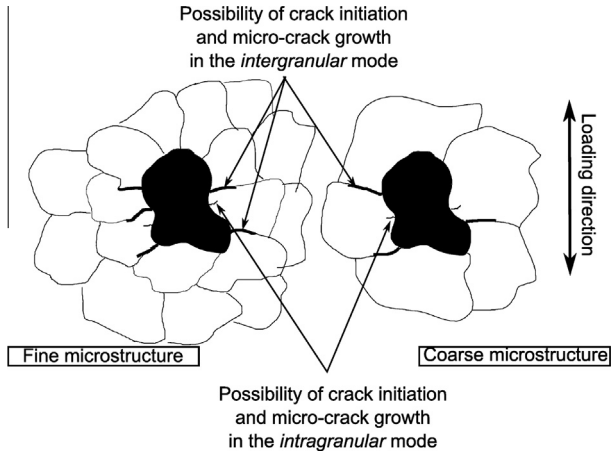
Fig. 11. Graphical illustration of the hypothesis concerning the influence of the grain size on the stress intensity threshold.

intensity threshold is modelled using the correction introduced by Koutiri et al. [8].

$$\frac{\Delta K_{th}|_R}{\Delta K_{th}|_{R=0}} = \frac{1-R}{1-\kappa R} \tag{25}$$

where κ is a material constant. The identification of this parameter needs the experimental fatigue strength corresponding to at least two different loading ratios R. Because only fatigue tests at a R-ratio of -1 were conducted, this parameter cannot be identified in the present work. Hence, the value of $\kappa = 0.59$ identified in the work of Koutiri et al. [8] is used in this modelling. This value was obtained by using the experimental uniaxial fatigue strength of alloy A with two load ratios ($R = -1$ and $R = 0.1$).

Concerning the uniaxial fatigue strength of alloy C with $R = 0.1$, only 4 fatigue tests have been carried out (2 failures and 2 run-outs). Hence, this data point should be considered only as a approximation of the uniaxial fatigue strength with $R = 0.1$.

From Fig. 12 it can be seen that:

- for the porosity free alloy (alloy C), good predictions are obtained for the $R = -1$ loading conditions (note that two of the three data points are identification points). However, the predictions for the $R = 0.1$ loading conditions are non-conservative.
- for the porosity-containing alloys, good agreement is observed for alloy A and the alloy studied by Bellett et al., except for the torsion loading condition. However, conservative predictions are generally shown for alloy B.
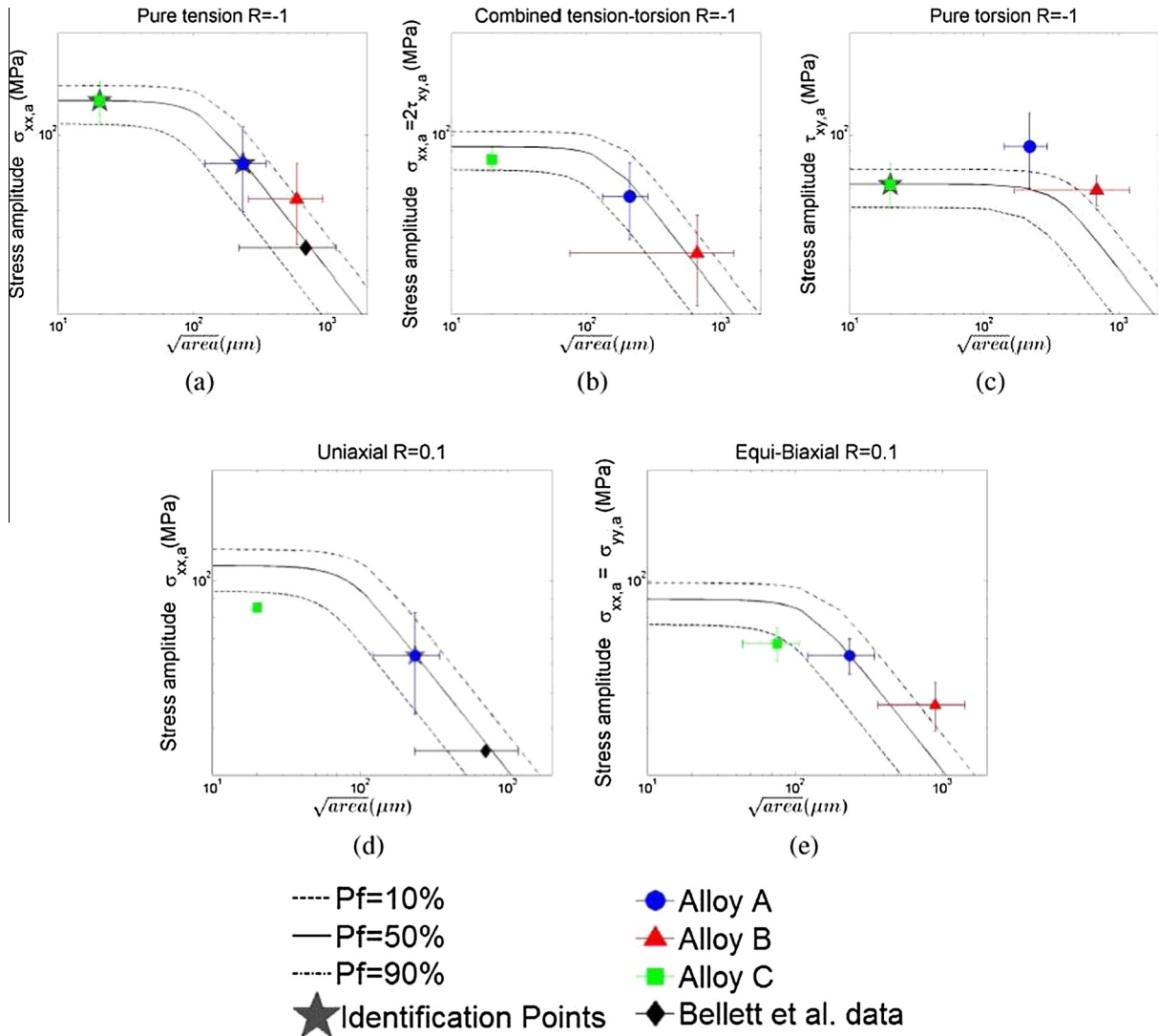

Fig. 12. Correlation between the experimental data and the model predictions using the Dang Van and the classical LEFM criteria.

One possible explanation for the conservative predictions for alloy B is that the value of ΔK_{th} used in the model is identified from the fatigue strength of alloy A, while these two alloys have significantly different SDAS and grain size values. As discussed in Section 4.2.2 an increase in SDAS has a beneficial effect on ΔK_{th}, in terms of crack growth from pores. Consequently, the following extension to the model is introduced in order to take into account this effect.

4.3.2. The Dang Van and *modified* LEFM criteria combination - taking into account the influence of the SDAS and the grain size

As per the classical LEFM criterion, the value of ΔK_{th} is assumed to be constant regardless of the microstructure. However, in this modified approach, a function of the SDAS $f(SDAS)$ is introduced and it is assumed that $\Delta K_{th}.f(SDAS)$ is constant. It must be kept in mind that because the SDAS and the grain size of the investigated alloys are correlated, the use of a function of the SDAS can also reflect the influence of the grain size on the ΔK_{th}.

As a first approach, it is proposed that $f(SDAS) = 1/\sqrt{SDAS}$ and that $\Delta K_{th}.f(SDAS)$ can be expressed by Eq. (26).

$$\Delta K_{th} f(SDAS) = \Delta K_{th} \frac{1}{\sqrt{SDAS}} = 2\sigma_a 0.65 \sqrt{\pi \frac{\sqrt{area}}{SDAS}} \qquad (26)$$

It is particularly interesting to note that thank to the proposed function $f(SDAS)$, a novel parameter, $\sqrt{area}/SDAS$ is introduced. This parameter can be considered as the relative defect size with respect to the microstructure. The application to alloys A and B gives the following: $\Delta K_{th,A}/\sqrt{SDAS_A} = 476$ MPa$\sqrt{m}/\sqrt{m}$ and $\Delta K_{th,B} 1/\sqrt{SDAS_B} = 450$ MPa$\sqrt{m}/\sqrt{m}$. The negligible difference ($\approx 5\%$) between these two values confirms the hypothesis that $\Delta K_{th} f(SDAS)$ is a constant.

Fig. 13 shows the predictions of the modified model.

It can be stated in Fig. 13 that the predictions related to the mechanism 2 are in a good agreement with the experimental data.

However, the large conservative or non-conservative predictions remain for certain cases related to the mechanism 1:

- For alloy A loaded in torsion ($R = -1$). This is because the modified model only takes into account the effect of the SDAS and grain size on mechanism 2 (i.e. crack growth from pores). Its effect on mechanism 1 has not been considered and the fatigue damage for alloy A under torsional loads is principally controlled by mechanism 1 even though the alloy contains pores [10]. Furthermore, the aluminium matrix of alloy A has higher resistance to shear stress when compared to alloy C as it contains a higher percentage of Copper [10]. This fact can be observed in Fig. 14 showing the comparison of the threshold of the resolved shear stress for the formation of PSB reported in the work of Le et al. [10]. Consequently, the Dang Van parameters identified using the data for alloy C (see Eqs. (21) and (22)) cannot correctly predict the torsional fatigue strength of alloy A.
- For alloy C loaded in uniaxial ($R = 0.1$) and in biaxial tension ($R = 0.1$). Because the Dang van coefficient α_{DV} is identified from the uniaxial $R = -1$ and torsional $R = -1$ loading conditions in which the principal fatigue damage mechanism is related to the formation of PSB, the crack initiation mechanism involving the rupture/debonding of eutectic particles observed for uniaxial $R = 0.1$ and equibiaxial tension $R = 0.1$ loads cannot be adequately modelled. One of possible explanations of this change of the fatigue damage mechanism is the increase of the maximum hydrostatic stress between the tension $R = 0.1$ load and the equibiaxial tension $R = 0.1$ load.

As a perspective to improve the predictions related to mechanism 1, a modification to the classical Dang-Van criterion is proposed. In order to take into account the addition of copper in the chemical compositions (for alloy A), it is proposed to make the Dang-Van parameter β a function of the micro-hardness of the alpha phase dendrites, $\beta = f(Hv)$. This approach has been used by Pessard et al. [30] for a Boron steel, in which $\beta = f(Hv)$ was chosen to be a linear function. Regarding the change in crack initiation mechanism observed when the maximum hydrostatic stress is increased, it is proposed that instead of using a unique coefficient α_{DV} to reflect the effect of the maximum hydrostatic stress as per the classical Dang-Van criterion (see Eq. (7)), two coefficients could be used to separately describe the effects of the mean and the amplitude of the hydrostatic stress. Eq. (27) shows the proposed modifications to the Dang-Van criteria.

$$\tau + \alpha\sigma_{H,a} + \gamma\sigma_{H,m} \leqslant f(Hv) \qquad (27)$$

where Hv is the micro-hardness of the aluminium matrix, $f(Hv)$ is a function of the micro-hardness that must be identified and α and γ are material parameters that must be identified. These identifications need more experimental work that will be conducted in the future project.

4.3.3. Prediction of the critical defect sizes

Thank to the Kitagawa-Takahashi diagrams shown in Fig. 13, the critical defect sizes for the different loading conditions and alloys can be predicted. The predicted critical defect sizes are considered as the intersection between the horizontal line (i.e. corresponding to the mechanism 1) and the inclined line (i.e. corresponding to the mechanism 2). Table 5 shows the relative defect size (i.e. as a function of the SDAS) as well as the absolute defect size, corresponding to the SDAS of alloys A and B. However, it must be kept in mind that because the predictions related to the mechanism 1 in some cases are not in a good agreement, the results shown in this section can be considered as a first rough estimation.

Some of these predicted values are in good agreement with the experimental observations in the literature: Brochu et al. [31] stated the critical defect size for uniaxial loads with $R = -1$ of $\sqrt{area} = 155$ µm for permanent mould A357 alloys with the SDAS is approximatively 60 µm. The relative critical pore size is thus $\sqrt{are}/SDAS \approx 2.6$, close to the predicted value here of 2.1. Concerning the torsion loads at $R = -1$, it is stated in the previous published work [10] a critical pore size of $\sqrt{area} = 450$ µm for alloy B and the predicted critical pore size here is 557 µm.

5. Conclusions

The principal aim of this paper was to develop a probabilistic model adapted to cast Al-Si alloys for the high cycle fatigue domain which is able to take into account different microstructural heterogeneities. The proposed model is based on the experimental fatigue strength data and observations of the fatigue damage mechanisms for different multiaxial loading conditions.

The principal conclusions of this work can be summarised as follows:

- The characterisation of the pore size thank to the extreme value inclusion rating methodology results in very different pore size distributions for the three investigated alloys. Furthermore, when using this methodology the predicted maximum defect size in a given volume (corresponding to the fatigue specimens) is in a good agreement with the defect size observed on the fatigue failure surfaces. This indicates the possibility of developing an approach which is able to take into account the volume effect on the fatigue strength of cast aluminium alloys.
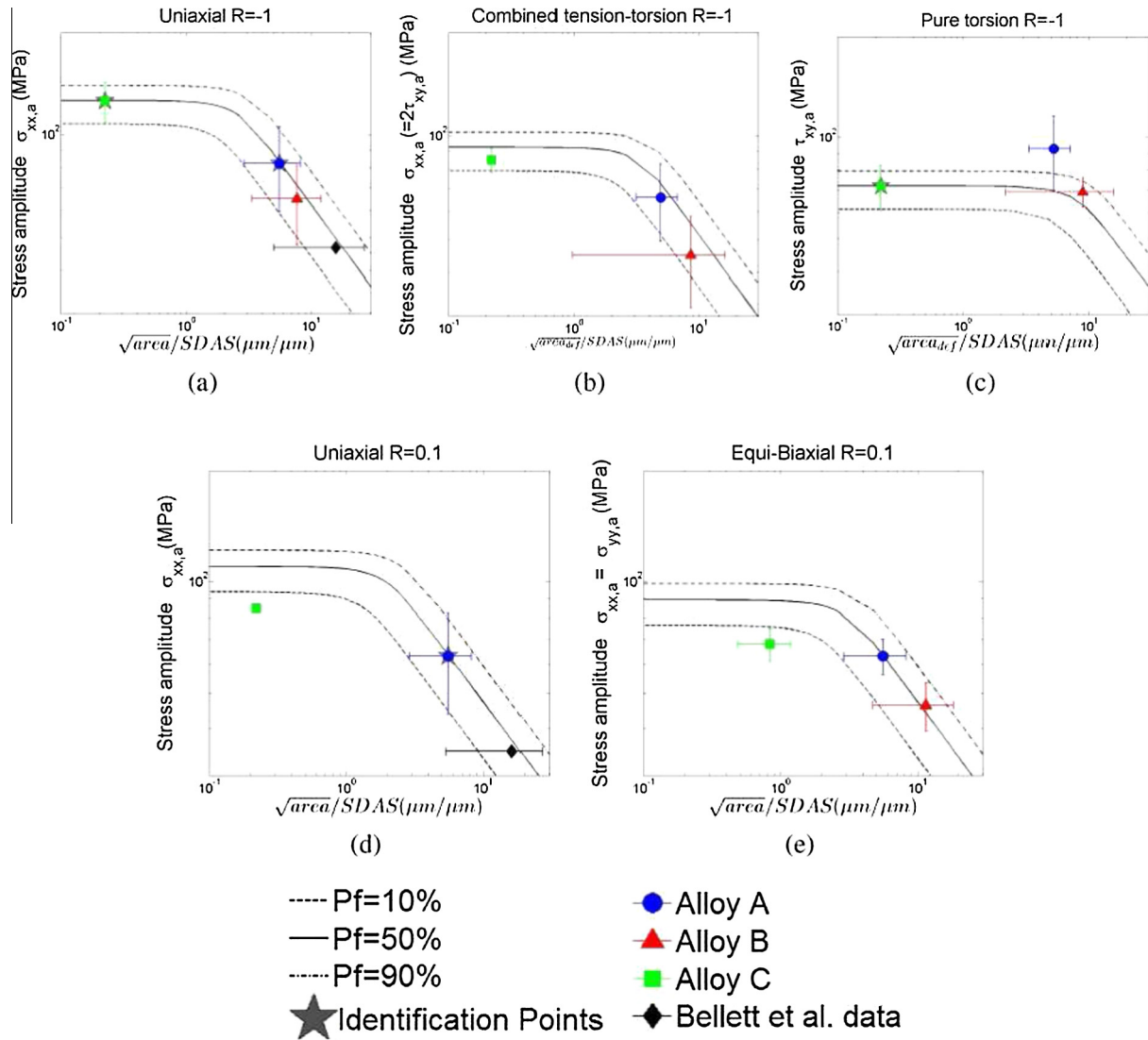
Fig. 13. Correlation between the experimental data and the model predictions combining the Dang Van and the **modified** LEFM criteria.
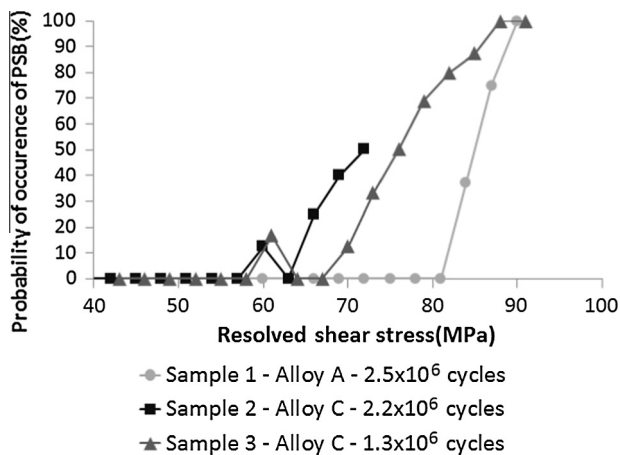

Fig. 14. Relationship between the probability of occurence of PSB and the maximum resolved shear stress [10].

- It is proposed that grain boundaries have several roles in terms of crack growth. In particular, it is proposed that the classical idea that grain boundaries act as microstructural barriers is only

Table 5
Prediction of the critical defect size for different loading conditions.

Loading conditions	Relative defect size	Absolute defect size $\sqrt{area}$ (μm)	
	$\sqrt{area}/SDAS$	Alloy A	Alloy B
Uniaxial with $R = -1$	2.1	106	184
Combined tension-torsion with $R = -1$	3.1	136	238
Pure torsion with $R = -1$	7.5	330	557
Uniaxial with $R = 0.1$	1.8	79	138
Equibiaxial tension with $R = 0.1$	2.7	119	207

true if the crack length exceeds the grain size. However, for early stage crack growth from pores, grain boundaries accelerate the growth rate and facilitate cracking. For the investigated cast Al-Si alloys investigated, because of the relatively large grain size compared to the pore size, an increase in the SDAS and grain size leads to an increase in the stress intensity threshold ΔK_{th}.

- The proposed model uses a combination of the Dang Van criterion and a modified LEFM criterion is able to take into account the effect of the microstructure on the mechanism of crack growth from pore (mechanism 2). Two modifications related to the classical Dang Van criteria are proposed in order to take into account, on one hand, the change of the microstructure (mainly in terms of the micro-hardness of the Al phase) and on the other hand, the change of the fatigue damage mechanism. These modifications need some addition material parameters which will be identified in the future work.

Acknowledgement

References

[1] Chan KS, Jones P, Wang Q. Fatigue crack growth and fracture paths in sand cast {B319} and {A356} aluminum alloys. Mater Sci Eng: A 2003;341(12):18–34. http://dx.doi.org/10.1016/S0921-5093(02)00196-X. Available from: <http://www.sciencedirect.com/science/article/pii/S092150930200196X> .

[2] Murali S, Arvind TS, Raman KS, Murthy KSS. Fatigue properties of sand cast, stircast and extruded Al7Si03Mg alloy with trace additions of Be and Mn. Mater Trans JIM 1997;38(1):28–36.

[3] McDowell D, Gall K, Horstemeyer M, Fan J. Microstructure-based fatigue modeling of cast A356-T6 alloy. Eng. Fract. Mech. 2003;70(1):49–80. http://dx.doi.org/10.1016/S0013-7944(02)00021-8. Available from: <http://www.sciencedirect.com/science/article/pii/S0013794402000218> .

[4] Gordon S-hC, Powell W, Mobley Carroll E. A fractography atlas of casting alloys. Battelle Press; 1992.

[5] Koutiri I. Effet des fortes contraintes hydrostatiques sur la tenue en fatigue des matériaux métalliques Ph.D. thesis. ENSAM; 2011.

[6] Buffière J-Y, Savelli S, Jouneau P, Maire E, Fougères R. Experimental study of porosity and its relation to fatigue mechanisms of model AlSi7Mg0.3 cast al alloys. Mater Sci Eng: A 2001;316(12):115–26. http://dx.doi.org/10.1016/S0921-5093(01)01225-4. Available from: <http://www.sciencedirect.com/science/article/pii/S0921509301012254> .

[7] Koutiri I, Bellett D, Morel F, Augustins L, Adrien J. High cycle fatigue damage mechanisms in cast aluminium subject to complex loads. Int J Fatigue 2013;47(0):44–57. http://dx.doi.org/10.1016/j.ijfatigue.2012.07.008. Available from: <http://www.sciencedirect.com/science/article/pii/S0142112312002356> .

[8] Koutiri I, Bellett D, Morel F, Pessard E. A probabilistic model for the high cycle fatigue behaviour of cast aluminium alloys subject to complex loads. Int J Fatigue 2013;47(0):137–47. http://dx.doi.org/10.1016/j.ijfatigue.2012.08.004. Available from: <http://www.sciencedirect.com/science/article/pii/S0142112312002472> .

[9] Huyen N, Flaceliere L, Morel F. A critical plane fatigue model with coupled meso-plasticity and damage. Fatigue Fract Eng Mater Struct 2008;31(1):12–28. http://dx.doi.org/10.1111/j.1460-2695.2007.01197.x.

[10] Le V-D, Morel F, Bellett D, Saintier N, Osmond P. Multiaxial high cycle fatigue damage mechanisms associated with the different microstructural heterogeneities of cast aluminium alloys. Mater Sci Eng: A 2016;649:426–40. http://dx.doi.org/10.1016/j.msea.2015.10.026. Available from: <http://www.sciencedirect.com/science/article/pii/S0921509315304901> .

[11] Pessard E. Comportement anisotrope en fatigue des conposants mcaniques forgs Ph.D. thesis. ENSAM; 2009.

[12] Pessard E, Morel F, Morel A. The anisotropic fatigue behavior of forged steel. Adv Eng Mater 2009;11(9):732–5. http://dx.doi.org/10.1002/adem.200900040.

[13] Pessard E, Bellett D, Morel F, Koutiri I. A mechanistic approach to the kitagawatakahashi diagram using a multiaxial probabilistic framework. Eng Fract Mech 2013;109:89–104. http://dx.doi.org/10.1016/j.engfracmech.2013.06.001. Available from: <http://www.sciencedirect.com/science/article/pii/S001379441300218X> .

[14] Pessard E, Morel F, Bellett D. Modelling the role of non-metallic inclusions on the anisotropic fatigue behaviour of forged steel. Int J Fatigue 2011;33(4):568–77. http://dx.doi.org/10.1016/j.ijfatigue.2010.10.012. Available from: <http://www.sciencedirect.com/science/article/pii/S0142112310002471> .

[15] Pessard E, Morel F, Verdu C, Flacelire L, Baudry G. Microstructural heterogeneities and fatigue anisotropy of forged steels. Mater Sci Eng: A 2011;529(0):289–99. http://dx.doi.org/10.1016/j.msea.2011.09.031. Available from: <http://www.sciencedirect.com/science/article/pii/S0921509311009919>.

[16] Murakami Y. Effects of small defects and nonmetallic inclusions. Elsevier; 2002.

[17] Dezecot S, Brochu M. Microstructural characterization and high cycle fatigue behavior of investment cast {A357} aluminum alloy. Int J Fatigue 2015;77:154–9. http://dx.doi.org/10.1016/j.ijfatigue.2015.03.004. Available from: <http://www.sciencedirect.com/science/article/pii/S0142112315000638> .

[18] Weibull W. A statistical theory of the strength of materials. Generalstabens litografiska anstalts frlag; 1939.

[19] Weibull W. A statistical distribution function of wide applicability. J Appl Mech 1951;18:293–7.

[20] Nguyen TTH. Effet des hétérogénéités microstructurales sur le comportement en fatigue multiaxiale a grand nombre de cycles Ph.D. thesis. Arts et Metiers ParisTech, Centre dAngers LPMI; 2008.

[21] Dang Van. Sur la resistance a la fatigue des metaux. Sciences et techniques de l'armement 1973;(47):641–772.

[22] Bellett D, Morel F. Influence des fortes contraintes hydrostatiques sur la rsistance en fatigue dun alliage daluminium as7g03u, Tech. rep., SERAM Centre d'Angers; 2005.

[23] Caton M, Jones J, Allison J. The influence of heat treatment and solidification time on the behavior of small-fatigue-cracks in a cast aluminum alloy. Mater Sci Eng: A 2001;314(12):81–5. http://dx.doi.org/10.1016/S0921-5093(00)01916-X. Available from: <http://www.sciencedirect.com/science/article/pii/S092150930001916X> .

[24] Caton MJ, Jones JW, Mayer H, Stanzl-Tschegg S, Allison JE. Demonstration of an endurance limit in cast 319 aluminum. Metall Mater Trans A 2003;34(11):33–41.

[25] Merhy E. Propagation de fissure sous chargement thermomécanique cyclique anisotherme: Application au dimensionnement de structures automobiles en alliage d'aluminum (Al-Si) Ph.D. thesis. Ecole Polytechnique de Paris; 2011.

[26] Skallerud B, Iveland T, Hrkegrd G. Fatigue life assessment of aluminum alloys with casting defects. Eng Fract Mech 1993;44(6):857–74. http://dx.doi.org/10.1016/0013-7944(93)90108-5. Available from: <http://www.sciencedirect.com/science/article/pii/0013794493901085> .

[27] Mbuya T, Sinclair I, Moffat A, Reed P. Micromechanisms of fatigue crack growth in cast aluminium piston alloys. Int J Fatigue 2012;42(0):227–37. http://dx.doi.org/10.1016/j.ijfatigue.2011.10.015. fatigue Damage of Structural Materials {VIII} Available from: <http://www.sciencedirect.com/science/article/pii/S0142112311002921> .

[28] Niklas A, Abaunza U, Fernandez-Calvo AI, Lacaze J, Suarez R. Thermal analysis as a microstructure prediction tool for A356 aluminium parts solidified under various cooling conditions, in: 69th World Foundry Congress (WFC), Hangzhou, China, 2011, pp. 89–95, this paper was published by the Foundry Journal Agency in the Chiny Foundry Journal, vol. 8 (n? 1). pp. 89–95. ISSN 1672-6421. <http://oatao.univ-toulouse.fr/5836/>.

[29] Munoz IS. Etude de l'influence des défauts de fonderie sur le comportement en fatigue de l'alliage aéronautique a357-t6 Ph.D. thesis. Institut National des Sciences Appliquées de Lyon; 2014.

[30] Pessard E, Abrivard B, Morel F, Abroug F, Delhaye P. The effect of quenching and defects size on the {HCF} behaviour of boron steel. Int J Fatigue 2014;68:80–9. http://dx.doi.org/10.1016/j.ijfatigue.2014.06.002. Available from: <http://www.sciencedirect.com/science/article/pii/S0142112314001637> .

[31] Brochu M, Verreman Y, Ajersch F, Bouchard D. High cycle fatigue strength of permanent mold and rheocast aluminum 357 alloy. Int J Fatigue 2010;32(8):1233–42. http://dx.doi.org/10.1016/j.ijfatigue.2010.01.001. Available from: <http://www.sciencedirect.com/science/article/pii/S0142112310000149> .